

Tin-containing Silicon Oxycarbonitride Ceramic Nanocomposites as Stable Anode for Magnesium Ion Batteries

Wuqi Guo,^[a] Jun Wang,^[a] Aleksander Gurlo,^[a] and Maged F. Bekheet^{*[a]}

The development of magnesium ion batteries as a viable alternative to lithium-ion batteries is impeded by the lack of efficient and stable electrode materials. Here, we present the synthesis of nanocomposites of tin-containing silicon oxycarbonitride (Sn/SiOCN) as anode materials for magnesium ion batteries (MIBs). The elemental and phase composition, morphology, and surface area of the nanocomposites are assessed by several characterization techniques. The galvanostatic cycling tests indicate a substantial initial discharging capacity for the anode with 42.2 wt.% of tin. Specifically, the first discharging capacities are 489.9 mA/g, 172.9 mA/g, and 136.6 mA/g at current densities of 0.5 mA/g, 50 mA/g, and 500 mA/g, respectively. After 100 cycles at a current density of

500 mA/g, the anode containing 33.8 wt% of tin exhibits a reversible capacity of 101.8 mAh/g and a remarkable rate performance efficiency of 76.5%. Increasing tin content in the electrode materials increases the battery performance by decreasing electrode impedance and thus facilitating Mg²⁺ diffusion, as revealed by electrochemical impedance spectroscopy (EIS). *Ex situ* XRD and X-ray photoelectron spectroscopy (XPS) characterizations following the magnesiation–demagnesiation process confirm the storage of reversible storage of Mg²⁺ ions in Sn/SiOCN electrode through incorporation in the SiOCN network and alloying/dealloying process involving Mg–Mg₂Sn–Mg.

Introduction

Post-lithium-ion batteries have been investigated in past decades due to several drawbacks of lithium ion batteries (LIBs), like the tendency for dendrite formation linked with safety concerns.^[1] Similar to LIBs in basic structure, magnesium ion batteries (MIBs) have been regarded as an alternative to replace LIBs in some fields, such as electric vehicles.^[2] In comparison with the geological availability of lithium, magnesium exists in the earth's crust with a high abundance (approximately 1.5 wt%).^[3] Besides, magnesium as an electrode in batteries has several superiorities, which include a superior theoretical volumetric energy density of 3833 mAh/cm³ (vs. 2046 mAh/cm³ for Li-metal anode) and a high gravimetric capacity of 2205 mAh/g, and a lower tendency for anodic dendrite formation, alleviating one of the key safety concerns associated with Li-ion batteries.^[4] Besides, a magnesium electrode has a strongly negative reduction potential of –2.3 V versus a standard hydrogen electrode.^[5]

Si and Sn, with theoretical capacities of 3600 mAh/g and 994 mAh/g to store Li⁺, respectively, have attracted much attention in the pursuit of finding suitable electrode materials with higher theoretical capacity to replace graphite (theoretical capacity to store Li⁺:372 mAh/g) in lithium-ion batteries (LIB).^[6–8] For other secondary batteries like sodium ion batteries (SIB) and magnesium ion batteries (MIB), Si and Sn also exhibit great electrode application possibilities.^[9,10] However, both electrode materials face severe problems, leading to poor battery performance. Silicon electrodes suffer from structural deterioration and poor performance stability due to their large volume expansion and pulverization during battery cycling, limiting their applications in batteries.^[11] In recent years, Si-containing polymer derived ceramics (PDCs), which are synthesized by pyrolyzing organosilicon polymers, have been introduced by researchers as an alternative for Si electrodes to prevent the above-mentioned problems.^[12] Silicon oxycarbide (SiOC) and silicon carbon nitride (SiCN), possessing unique microstructures compared with other ceramic materials, are two typical PDCs that have been investigated as electrodes in the field of rechargeable batteries.^[13] This material can be produced on a large scale and consists of nanodomains that are surrounded by free carbon.^[14] Encapsulating silica domains by viscoelastic free carbon or graphene cages in these PDCs materials could prevent their large expansion and contraction during battery cycling.^[15] Besides, the free carbon layers in the PDCs could provide host sites for ion storage and enhance electrical conductivity.^[16] Like silicon electrodes, metallic Sn electrodes also experience a large volume expansion and particle aggregation during charging/discharging, leading to poor cycling stability of the battery.^[17] Previous works reported

[a] W. Guo, J. Wang, A. Gurlo, Dr.-Ing. M. F. Bekheet

Technische Universität Berlin, Faculty III Process Sciences, Institute of Materials Science and Technology, Chair of Advanced Ceramic Materials, Straße des 17. Juni 135, 10623 Berlin, Germany
E-mail: maged.bekheet@ceramics.tu-berlin.de

 Supporting information for this article is available on the WWW under <https://doi.org/10.1002/batt.202400032>

 © 2024 The Authors. *Batteries & Supercaps* published by Wiley-VCH GmbH. This is an open access article under the terms of the Creative Commons Attribution License, which permits use, distribution and reproduction in any medium, provided the original work is properly cited.

that embedding metallic Sn nanoparticles in SiOC and SiCN ceramics matrix could buffer their volume expansion and agglomeration during the cycling of lithium ion batteries.^[18–22] The stable and open network structure of the synthesized Sn/SiOC and Sn/SiCN nanocomposites could alleviate the capacity fading of Sn caused by volume expansion during the charging/discharging process.^[23] In addition, the electrical conductivity of these nanocomposites could be greatly increased because of the high electrical conductivity of tin (91000 S/cm) compared with that of SiOC/SiCN, thus improving the corresponding battery performance.^[7]

Although Sn/SiOC and Sn/SiCN have been applied as electrodes of rechargeable lithium ion batteries with good results in a few reports,^[18–22] they have not been tested as an anode for magnesium ion batteries before our recently published work.^[24] Our previous study showed Sn/SiOC nanobeads could be promising anode materials for magnesium ion batteries, possessing a high capacity of 198.2 mAh/g after the first discharging and a reversible capacity of 144.5 mAh/g after 100 cycles at 500 mA/g. Although our latter study showed that the battery performances were influenced by the tin content in the SiOC/Sn nanobeads, the synthesis route applied in this work did not allow us to increase the Sn and free carbon content above 6.3 wt.% and 31.6 wt.% of anode material, respectively. Thus, in this research, Sn/SiOCN nanocomposites with uniform distributions of Sn nanoparticles and high amounts of Sn/free carbon contents (up to 42.4 wt.%) were synthesized with the method reported in our previously published articles.^[22,25] In this synthesis route, several metal nanoparticles were *in situ* formed during the reaction of poly(vinyl) silazane (Durazane 1800) with metal acetates, leading to uniform distributions of metal nanoparticles in the SiOCN matrix after the pyrolysis step. The metal content can be controlled by varying the weight ratio of the polymer/metal acetate during the synthesis, while the free carbon content can be increased by crosslinking the polymer with another carbon-rich polymer (i.e., divinylbenzene (DVB)). Moreover, the use of polysilazane polymers in this work instead of polysiloxane polymers could introduce nitrogen in the SiOC matrix, improving the electrochemical performance of carbon-based materials due to their higher electronegativity in comparison with carbon.^[26] The synthesized materials were, for the first time, applied as anodes in magnesium batteries. The influences of Sn and free carbon contents on the electrochemical performance of Sn/SiOCN ceramic nanocomposites are evaluated by testing the magnesiation-demagnesiation capacity at different current densities, rate capability, and cycling stability. Moreover, their electrochemical kinetics are studied by cyclic voltammetry (CV) at different scan rates and electrochemical impedance spectroscopy (EIS) before/after cycling. At last, the magnesium ion storage mechanism with Sn and the theoretical capacity of the synthesized materials were investigated by ex-situ X-ray diffraction (XRD) and X-ray photoelectron spectroscopy (XPS).

Experimental Section

Materials

Poly(vinyl)silazane (Durazane 1800, durXtreme GmbH, Germany), tin (II) acetate (99%, Sigma-Aldrich, Germany), divinylbenzene (DVB, technical grade, 80%, Aldrich), anhydrous tetrahydrofuran (THF, 99%, Sigma-Aldrich, Germany), and platinum Karstedt's catalyst (platinum (0)-1,3-divinyl-1,1,3,3-tetramethyldisiloxane complex solution in xylene, Pt≈2%, Sigma-Aldrich) were used for the synthesis of Sn-containing polysilazane precursors that were subsequently pyrolyzed to ceramics as described below.

For battery testing, nickel (99.9%) and magnesium (99.9%) foils were acquired from Goodfellow. Phenylmagnesium chloride solution (PhMgCl; 2.0 M in THF), anhydrous AlCl₃ and Whatman® glass fiber filter paper (GF/A) were ordered from Sigma Aldrich. Carbon black, anhydrous tetrahydrofuran (THF), 1-Methyl-2-pyrrolidinone (NMP) and polyvinylidene difluoride (PVDF) were purchased from Alfa Aesar. Coin cell cases (CR2032) were obtained from Mitsubishi.

The Synthesis of Sn/SiOCN Nanocomposites

In this study, we investigate the tin-containing ceramic SiOCN nanocomposites that we synthesized and reported in our previous work, where we characterized them as anodes for lithium-ion batteries.^[22] In contrast to our previous work, here we perform an additional complementary characterization necessary for understanding their structure, composition, and performance as anodes for magnesium-ion batteries. A brief summary of the synthesis procedure from ref.^[22] is as follows: 2 g poly(vinyl)silazane (Durazane 1800) polymer was mixed with various amounts of anhydrous tin acetate Sn(Ac)₂ (i.e., 0.8, 1.4, 3.0, and 4.2 g) using anhydrous THF (50 mL) as a solvent. The obtained solution mixture was placed immediately in an ice bath until the reaction between the polymer and Sn(Ac)₂ was completed under argon flow and stirring. The obtained precursor solution was stirred for a further 24 hours at room temperature before adding 0.01 mL Karstedt's platinum catalyst and 1 g DVB and increasing the temperature to 50 °C for an additional 24 hours to obtain the gel precursor. Lastly, the THF solvent residue was evaporated under a vacuum to get the dried Sn-containing precursors to be pyrolyzed in Schlenk tube at 1000 °C for 3 hours under argon flow. The obtained ceramic materials after pyrolysis were denoted as SiOCN, Sn_{13.8}SiOCN, Sn_{20.1}SiOCN, Sn_{33.8}SiOCN, and Sn_{42.4}SiOCN, where the numbers following Sn (0, 13.8, 20.1, 33.8, 42.4) in the samples name refer to the elemental weight percent of Sn in the samples, as revealed by elemental analysis (see Table 1).

Characterization

To confirm the phase composition of the specimens, reported previously,^[22] X-ray diffraction (XRD) analysis was conducted in a Bruker D8 diffractometer (AXS D8 ADVANCE X-ray diffractometer, Bruker, Billerica, MA, USA) equipped with CuK α radiation ($\lambda = 0.154$ nm) over 20 range from 20° to 90° using step counting time of 3 s and scanning rate of 0.05°. In the ref.^[22] the XRD analysis was performed with CoK α radiation.

Scanning electron microscopy (SEM) images were acquired using the equipment (ZEISS GEMINI SEM500 NanoVP, ZEISS, Jena, Germany) coupled with an energy dispersive X-ray detector (Bruker Quantax Xflash6, Bruker, Billerica, MA, USA) for EDS mapping. BSD4 detector was used for the characterization.

Transmission electron microscopy (TEM) investigation was performed in our previous work,^[22] and here we report additional

Table 1. The chemical composition of the samples calculated from the elemental analyses data adapted from our previous work, ^[22] as listed in Table S1).						
Samples	Chemical formula $\text{SiO}_x\text{C}_y\text{N}_z$	Weight fraction (wt. %)				
		SiO_2	SiC	Si_3N_4	C_{free}	Sn
SiOCN	$\text{SiO}_{0.25}\text{C}_{1.88}\text{N}_{0.97}$	11.2	8.2	50.0	30.6	0.0
$\text{Sn}_{13.8}\text{SiOCN}$	$\text{SiO}_{0.57}\text{C}_{3.58}\text{N}_{0.65}$	16.7	8.7	22.0	38.8	13.8
$\text{Sn}_{20.1}\text{SiOCN}$	$\text{SiO}_{0.88}\text{C}_{4.89}\text{N}_{0.21}$	20.5	12.3	5.7	41.4	20.1
$\text{Sn}_{33.8}\text{SiOCN}$	$\text{SiO}_{1.16}\text{C}_{4.50}\text{N}_{0.05}$	22.9	9.9	1.3	32.1	33.8
$\text{Sn}_{42.4}\text{SiOCN}$	$\text{SiO}_{1.70}\text{C}_{3.78}\text{N}_{0.03}$	29.3	2.9	0.5	24.9	42.4

complementary data. A brief summary of the characterization procedure from ref.^[22] is given below. TEM characterization was performed in FEI Tecnai G² 20 S-TWIN equipped with a LaB6-source at 200 keV acceleration voltage (FEI, USA). The samples for TEM analysis were prepared by dispersing the samples powder in anhydrous THF, followed by dropping them onto a copper grid covered with carbon film. Particle size distribution was calculated from TEM images with Nano measurer by quantifying 100 particles.

We use the data of the elemental analyses from our previous work^[22] (see Supporting Information) to calculate the chemical composition of the samples. As reported previously,^[22] elemental analysis for silicon (Si) and tin (Sn) was performed with inductively coupled plasma optical emission spectroscopy (ICP–OES) by using a Horiba Scientific ICP Ultima2 (Horiba, Kyoto, Japan). Prior to analyses, powder samples were digested in an aqueous suspension of HNO_3 and HF acids mixture at 200 °C for 5 h in a Teflon-lined autoclave. Elemental carbon, nitrogen, and oxygen contents in the synthesized samples were determined by a carbon analyzer CS744 (Leco Corporation, USA) and an N/O analyzer Leco ON–836 (Leco Corporation, USA). The chemical composition of synthesized materials was normalized to 1 Si (i.e., $\text{SiO}_x\text{C}_y\text{N}_z$). The mole fraction of SiC , SiO_2 , Si_3N_4 and C_{free} in the samples was calculated considering the composition of the synthesized samples as $(\frac{x}{2})$ mol SiO_2 , $(\frac{z}{4})$ mol Si_3N_4 , $(1 - \frac{x}{2} - \frac{z}{4})$ mol SiC and $(y - 1 + \frac{x}{2} + \frac{z}{4})$ mol C_{free} .^[27]

Nitrogen sorption was applied using a QuadraSorb Station 4 apparatus (Quantachrome, Boynton Beach, FL, USA). Isotherms were recorded at 77 K after degassing under a vacuum at 200 °C for 24 h before the measurement. The specific surface area (SSA) was acquired using Brunauer–Emmett–Teller (BET) calculations.

X-ray photoelectron spectroscopy (XPS) measurements were conducted on an ESCALAB 250Xi instrument (Thermo Fisher Scientific, Waltham, MA, USA). The X-ray spot size was 100 nm. Powders were sprinkled on the carbon conductive tape in the glove box to prepare samples for analysis. The C 1s core line with a binding energy of 284.8 eV was used to calibrate all XPS spectra. The data were processed by using XPS Peak software. The Lorentzian–Gaussian ratios in peak fitting have been constrained between 20 and 30. Shirley backgrounds were used in all fittings.

Battery assembling procedures were conducted in an argon-filled glove-box under an inert atmosphere. Coin cell cases, spacers, springs and o-rings produced by Mitsubishi® were used. A slurry of 80 wt.% active material, 10 wt.% Super-P carbon back and 10 wt.% polyvinylidene fluoride dispersed in N-methyl-2-pyrrolidone (NMP) were prepared by wet grinding for 1 h. For fabrication of the working electrodes, this slurry was then tape–cast on nickel foil and dried, first in air at 50 °C, and then under vacuum at 100 °C. The resulting mass loading of the active material was 1 mg/cm². The coated working electrodes were then pressed at a pressure of 80–120 kg/cm² and were cut into circular forms of 12 mm in diameter. Magnesium foil with a diameter of 14 mm and a thickness

of 0.25 mm was adopted as the counter electrode. Whatman® glassfibre filter paper (GF/A) was adopted as a cell separator.

The electrolyte was synthesized in a glove-box under argon following the procedure described in elsewhere.^[24,28] First, 1.34 g AlCl_3 was added slowly to 40 mL THF solvent under vigorous stirring to obtain the targeted concentration. Subsequently, the acquired solution was dropwise added to a 10 mL PhMgCl/THF solution (2 M PhMgCl), followed by stirring for 16 h at room temperature. The process of electrolyte preparation is exothermic.

Battery performance tests were conducted using a CT2001 A battery tester system (Wuhan LAND, Wuhan, China). Galvanostatic discharge–charge measurements were conducted in the potential range 0.05–2 V versus Mg^{2+}/Mg . Data points were collected every 3 seconds. The battery cycling stability tests were conducted at a current density of 500 mA/g for 100 cycles. The following current densities were applied for the rate capability tests: 5×50 mA/g, 5×100 mA/g, 5×200 mA/g, and 5×500 mA/g followed by 5×50 mA/g.

Cyclic voltammetry (CV) tests were carried out in assembled coin cells on a CHI660D electrochemical workstation (Chenhua, Shanghai, China) in the potential range of 0–2 V and at the scanning rate of 0.1 mV/s, 0.5 mV/s, 1.0 mV/s, 2.0 mV/s and 5.0 mV/s.

Electrochemical impedance spectroscopy (EIS) measurements were conducted on coin cells with all anode materials using a Gamry EIS box (Gamry, PA, USA) in potentiostatic mode with 5 mV amplitude between 50 mHz and 1 MHz. The measurements were conducted before the 1st cycle and after the 100 cycle, respectively. The cycling was conducted at 50 mA/g. Before the EIS measurements, the cells were discharged and charged with pausing intervals at certain cell potentials (0.5, 1.0, 1.5 and 2.0 V) and were relaxed for three hours.

To investigate the storage mechanism, the *ex-situ* XRD patterns on the electrode materials after stopping the battery cycling and taking out cathodes during the discharging (2 V, 0.3 V, 0.2 V, 0.1 V and 0 V) and charging (0 V, 0.1 V, 0.2 V, 0.3 V and 2 V) process.

Results and Discussion

Figure 1(a) presents the XRD patterns of the obtained ceramic samples after the pyrolysis process. The bare SiOCN ceramic shows an amorphous structure, which agrees with previous works showing that the SiOC retains its amorphous structure up to 1100 °C.^[21,22,25] The crystallization of SiOCN into SiC usually starts at 1200 °C.^[29] In contrast, the characteristic XRD reflections corresponding to crystalline metallic Sn (space group $I4_1/\text{amd}$ (PDF#00–089–2958)) are observed in the XRD patterns of all Sn-containing samples (i.e., $\text{Sn}_{13.8}\text{SiOCN}$, $\text{Sn}_{20.1}\text{SiOCN}$, $\text{Sn}_{33.8}\text{SiOCN}$,

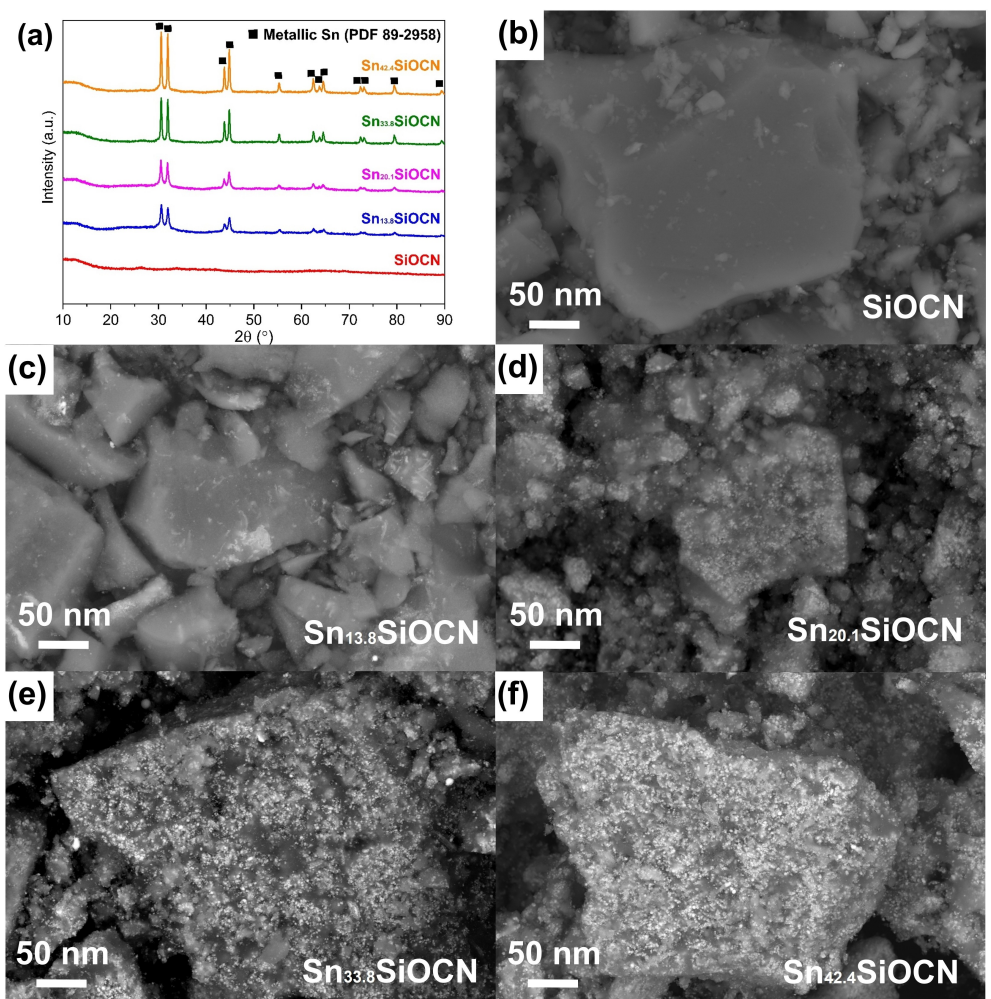


Figure 1. (a) XRD patterns of the synthesized ceramic nanocomposites with different tin content. (b–f) SEM images of SiOCN, Sn_{13.8}SiOCN, Sn_{20.1}SiOCN, Sn_{33.8}SiOCN and Sn_{42.4}SiOCN.

and Sn_{42.4}SiOCN). The crystallite size of metallic Sn, estimated from peak broadening using the Scherrer equation, is 21.5 ± 1 nm, 25.3 ± 1 nm, 29.7 ± 1 nm, and 31.9 ± 1 nm for Sn_{13.8}SiOCN, Sn_{20.1}SiOCN, Sn_{33.8}SiOCN, and Sn_{42.4}SiOCN, respectively. This increase in the crystallite size with increasing the tin content within the SiOCN ceramic matrix can be explained by the agglomeration of Sn nanoparticles at a high content in the matrix. Figure 1(b–f) present SEM images of SiOCN, Sn_{13.8}SiOCN, Sn_{20.1}SiOCN, Sn_{33.8}SiOCN and Sn_{42.4}SiOCN samples. There is no obvious change in the surface morphology of samples, except the increase in the amount and size of tin nanoparticles on the surface (i.e., bright spots in the SEM images) with increasing tin content in the samples. These results confirm the XRD results suggest the agglomeration of Sn nanoparticles at high content in the matrix. However, for SiOCN, Sn_{13.8}SiOCN, Sn_{20.1}SiOCN and Sn_{33.8}SiOCN, the tin aggregation phenomenon is not severe and the nanoparticle distribution could be seen as roughly uniform. For Sn_{42.4}SiOCN, obvious tin agglomeration becomes very dominant. SEM–EDX mapping characterization further confirmed this observation, as shown in (Figure 2). For every

sample, a roughly smooth plane was selected for the SEM–EDX mapping characterization.

The morphology and particle size of Sn nanoparticles within the amorphous SiOCN matrix were further investigated by TEM characterization. As shown in Figure 3, spherical Sn nanoparticles of about 30–50 nm can be observed in both Sn_{33.8}SiOCN and Sn_{42.4}SiOCN samples. This particle size estimated from TEM images is consistent with the crystallite size calculated from XRD analysis. However, the Sn_{42.4}SiOCN sample contains several larger particles (> 50 nm) due to the Sn agglomeration, agreeing with XRD, SEM, and EDS results. The results indicate the tin particle aggregation phenomenon could be well hindered in the SiOCN matrix when the tin weight content is less than or equal to 33.8 ± 0.2 wt %.

Table 1 shows the elemental analysis results for all synthesized ceramic nanocomposites. The chemical formula $\text{SiO}_x\text{C}_y\text{N}_z$ normalized to Si is quantified based on the reference.^[27] As displayed in Table 1, all samples except SiOCN contain a noticeable amount of Sn, which is in accordance with XRD, SEM, and EDS results shown in Figure 1. Increasing the tin content in the materials decreases the weight fraction of

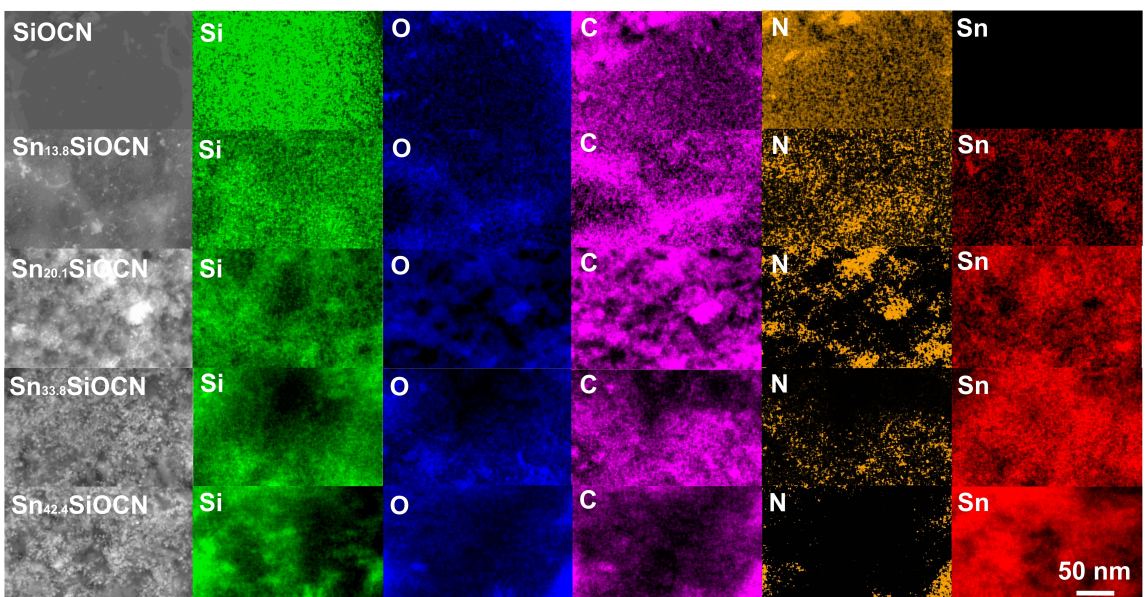


Figure 2. SEM and EDX mapping of SiOCN, $\text{Sn}_{13.8}\text{SiOCN}$, $\text{Sn}_{20.1}\text{SiOCN}$, $\text{Sn}_{33.8}\text{SiOCN}$ and $\text{Sn}_{42.4}\text{SiOCN}$.

elemental nitrogen and silicon while the oxygen content increases. Thus, the weight fraction of SiO_2 increases while the amount of Si_3N_4 decreases with the increase in Sn content. These results are expected since acetate groups of $\text{Sn}(\text{Ac})_2$ might react with the $-\text{Si}-\text{H}$ and $-\text{Si}-\text{NH}-\text{Si}-$ groups of Durazane 1800, forming $-\text{Si}-\text{OCOCH}_3$ side chain and releasing gaseous H_2 and NH_3 , respectively.^[21,22] In contrast, the amount of elemental carbon, SiC and free carbon increase first when low amounts of $\text{Sn}(\text{Ac})_2$ are used in the synthesis to produce $\text{Sn}_{13.8}\text{SiOCN}$ and $\text{Sn}_{20.1}\text{SiOCN}$ nanocomposites, indicating the complete reaction between the tin acetate and polymer as well as the increased extent of polymer crosslinking owing to the existence of tin acetate.^[21] However, when high amounts of $\text{Sn}(\text{Ac})_2$ are used to synthesize $\text{Sn}_{33.8}\text{SiOCN}$ and $\text{Sn}_{42.4}\text{SiOCN}$

samples, the total amount of elemental C, SiC, and free carbon decreases again with tin content, indicating that not all $\text{Sn}(\text{Ac})_2$ could react with the polymer; thus, high amounts of carbon are lost during the pyrolysis from the polymer or from unreacted Sn acetate. Thus, the weight fraction of Sn increases in the $\text{Sn}_{33.8}\text{SiOCN}$ and $\text{Sn}_{42.4}\text{SiOCN}$ samples while the carbon amount decreases.

Figure S1 shows the N_2 physisorption isotherms of SiOCN, $\text{Sn}_{13.8}\text{SiOCN}$, $\text{Sn}_{20.1}\text{SiOCN}$, $\text{Sn}_{33.8}\text{SiOCN}$ and $\text{Sn}_{42.4}\text{SiOCN}$ samples. All samples exhibit reversible Type IV isotherms based on IUPAC classification. In addition to the hysteresis loops, all samples show increased N_2 adsorption at high relative pressure ($p/p_0 > 0.8$). The calculated BET specific surface area (SSA) of $\text{Sn}_{13.8}\text{SiOCN}$ ($12 \pm 1 \text{ m}^2/\text{g}$), $\text{Sn}_{20.1}\text{SiOCN}$ ($15 \pm 1 \text{ m}^2/\text{g}$), and

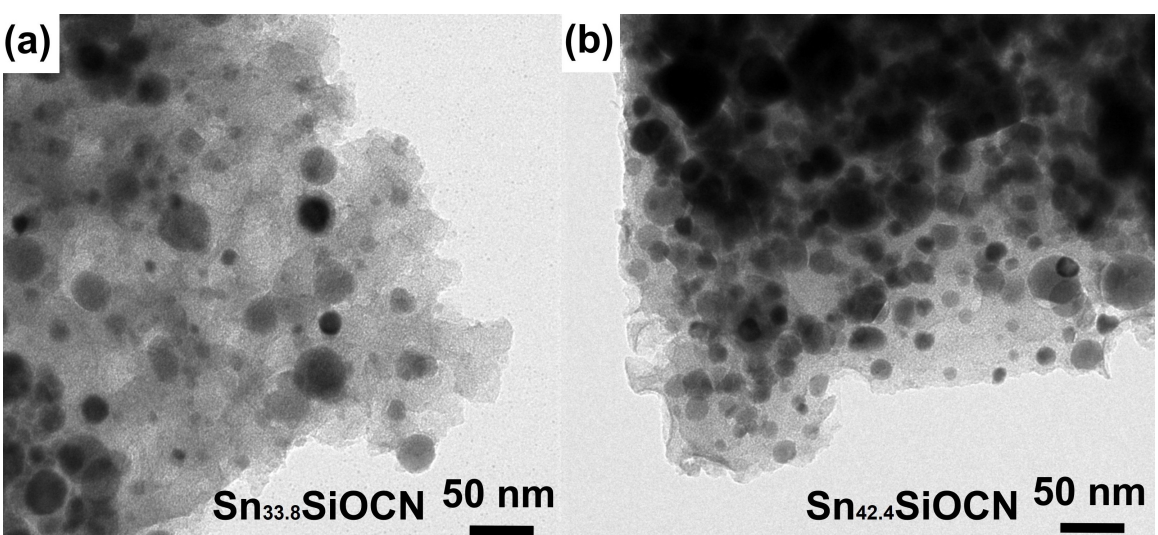


Figure 3. TEM images of $\text{Sn}_{33.8}\text{SiOCN}$ (a) and $\text{Sn}_{42.4}\text{SiOCN}$ (b).

$\text{Sn}_{33.8}\text{SiOCN}$ ($13 \pm 1 \text{ m}^2/\text{g}$) was higher than that of the SiOCN ($6 \pm 1 \text{ m}^2/\text{g}$) and $\text{Sn}_{42.4}\text{SiOCN}$ ($8 \pm 1 \text{ m}^2/\text{g}$). The lower surface area of $\text{Sn}_{42.4}\text{SiOCN}$ nanocomposite compared with other Sn-containing SiOCN nanocomposite might be explained by the agglomeration of Sn nanoparticles (see Figure 3) that might block the pores on the sample surface.

Figure 4 illustrates the results of the electrochemical tests of the obtained ceramics (SiOCN , $\text{Sn}_{13.8}\text{SiOCN}$, $\text{Sn}_{20.1}\text{SiOCN}$,

$\text{Sn}_{33.8}\text{SiOCN}$, and $\text{Sn}_{42.4}\text{SiOCN}$) as anodes for magnesium batteries. Figure 4(a–c) depicts the first cycle galvanostatic half-cell (Mg/anode) magnesiation–demagnesiation curves of SiOCN , $\text{Sn}_{13.8}\text{SiOCN}$, $\text{Sn}_{20.1}\text{SiOCN}$, $\text{Sn}_{33.8}\text{SiOCN}$ and $\text{Sn}_{42.4}\text{SiOCN}$ electrodes in the 0–2 V (vs. Mg^{2+}/Mg) voltage window at 0.5 mA/g, 50 mA/g and 500 mA/g. Three observable voltage regions for the storage of Mg^{2+} ions in all Sn-containing SiOCN electrodes. The two sloping voltage regions at low (<0.15 V) and high voltage

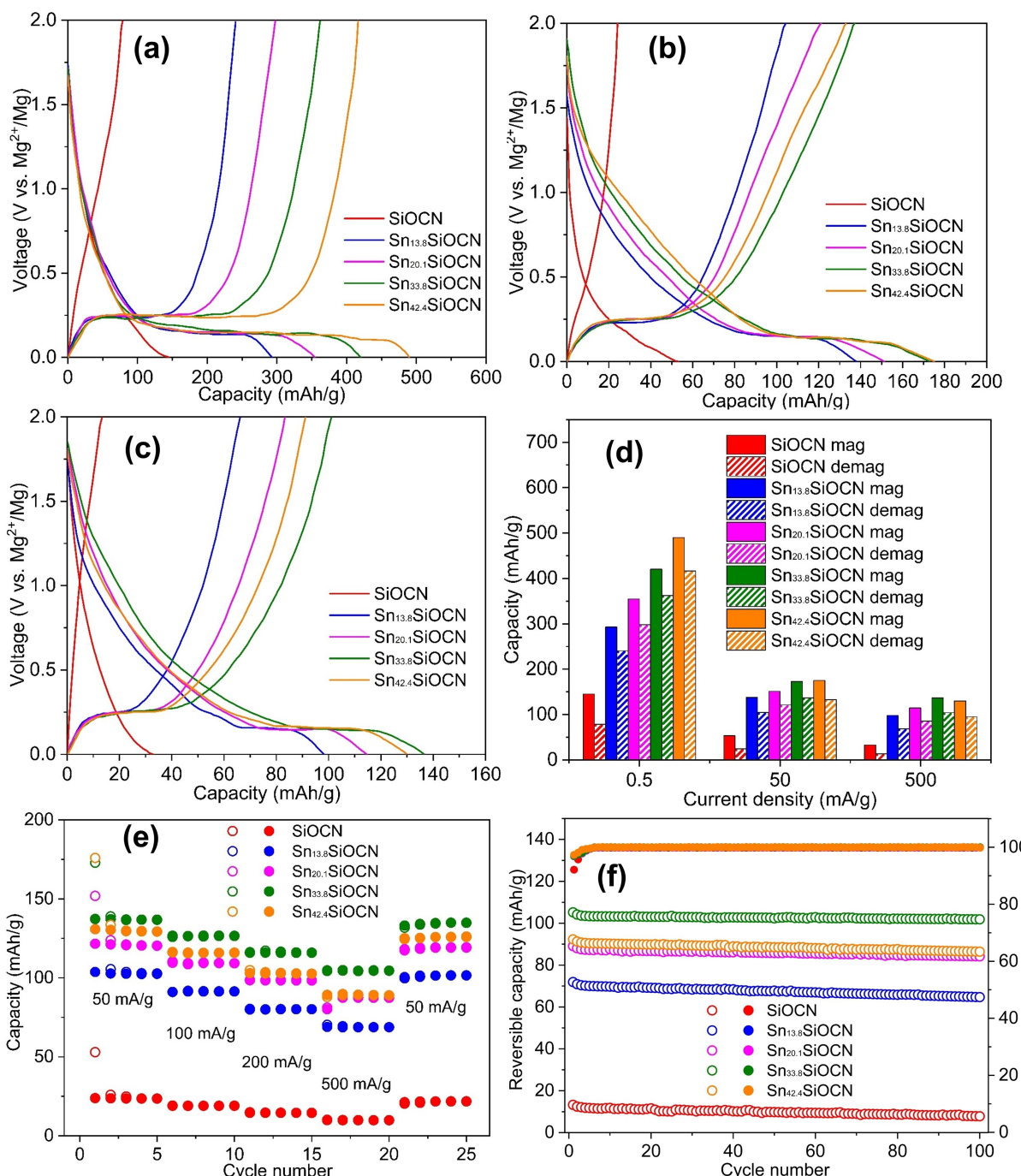


Figure 4. (a–c) Magnesiation–demagnesiation profiles of SiOCN , $\text{Sn}_{13.8}\text{SiOCN}$, $\text{Sn}_{20.1}\text{SiOCN}$, $\text{Sn}_{33.8}\text{SiOCN}$ and $\text{Sn}_{42.4}\text{SiOCN}$ at current density of 0.5 mA/g, 50 mA/g, and 500 mA/g; (d) Magnesiation and demagnesiation capacity of SiOCN , $\text{Sn}_{13.8}\text{SiOCN}$, $\text{Sn}_{20.1}\text{SiOCN}$, $\text{Sn}_{33.8}\text{SiOCN}$ and $\text{Sn}_{42.4}\text{SiOCN}$ at different current densities; (e) Rate capability tests of SiOCN , $\text{Sn}_{13.8}\text{SiOCN}$, $\text{Sn}_{20.1}\text{SiOCN}$, $\text{Sn}_{33.8}\text{SiOCN}$ and $\text{Sn}_{42.4}\text{SiOCN}$ at different current rates; (f) Cycling stability tests of SiOCN , $\text{Sn}_{13.8}\text{SiOCN}$, $\text{Sn}_{20.1}\text{SiOCN}$, $\text{Sn}_{33.8}\text{SiOCN}$ and $\text{Sn}_{42.4}\text{SiOCN}$ at a current density of 500 mA/g (open and solid spheres refer to reversible capacity and coulombic efficiency, respectively).

(>0.25 V) observed in all electrodes can be assigned to the insertion of Mg²⁺ ions into the micropores, defect sites, active chemical constituents, and between carbon layers of SiOCN materials,^[24,30] while the plateau region between 0.15 and 0.25 V observed for only the Sn-containing electrodes could be attributed to formation of Mg₂Sn alloy.^[31,32] Irreversible reaction of Mg²⁺ ions with Sn is confirmed by the difference between the de-magnesiation ($C_{mag.}$) and magnesiation capacities ($C_{mag.}$) in the first cycle; the irreversible capacity is denoted as C_{irr} . The ratio of $C_{demag.}$ and $C_{mag.}$ in the first cycle is known as the first cycle capacity retention rate η_{cr} (i.e., $C_{demag.1}/C_{mag.1} \times 100\%$),^[13,22] and their values are summarized in Table 2 and illustrated in Figure 4(d).

As shown in Table 2, the bare SiOCN electrode possesses magnesiation capacity of 145.2 mAh/g, 53.2 mAh/g, and 32.9 mAh/g in the first cycle at the current rate of 0.5 mA/g, 50 mA/g and 500 mA/g, respectively. Besides, the capacity retention rate η_{cr} of this electrode at the first cycle is very low (i.e., 40.4%–54.2%). All Sn/SiOCN electrodes display better electrochemical performance than the bare SiOCN electrode. Among them, the Sn_{42.4}SiOCN electrode presents the highest first magnesiation and demagnesiation capacity of 489.9 mAh/g and 416.4 mAh/g, respectively, at the current rate of 0.5 mA/g. However, the capacity retention rate η_{cr} of Sn_{42.4}SiOCN electrode at the first cycle is 85%, slightly lower than that of Sn_{33.8}SiOCN electrode (86.2%). The expected magnesiation capacity of Sn/

SiOCN nanocomposites at a current density of 0.5 mA/g can be calculated from the weight fraction of Sn and SiOCN in the composite, taking into account the theoretical capacity of Mg₂Sn (903 mAh/g) and the measured capacity of Sn_{free} SiOCN matrix (145.2 mAh/g). The capacities for Sn_{13.8}SiOCN, Sn_{20.1}SiOCN, Sn_{33.8}SiOCN, and Sn_{42.4}SiOCN nanocomposites are 249.8, 297.5, 401.3, 465.0 mAh/g, respectively, which are very close to the measured values for all specimens (see Table 2). The slightly higher experimental values can be explained by the enhanced electronic conductivity and surface area and increased free carbon content in the Sn/SiOCN nanocomposites by incorporating metallic tin nanoparticles within the amorphous SiOCN matrix.^[22,24] Thus, the highest difference between the estimated and measured magnesiation capacity of 43.2 mAh/g and 57.0 mAh/g is observed for Sn_{13.8}SiOCN and Sn_{20.1}SiOCN, respectively, which possess the highest surface and contain the highest amount of free carbon (see Table 1).

With increasing the current rate to 50 mA/g, the magnesiation capacity of all electrodes decreases, but the Sn_{42.4}SiOCN electrode still possesses the highest magnesiation capacity of 175.2 mAh/g, which is slightly higher than that of Sn_{33.8}SiOCN electrode (172.9 mAh/g). However, the capacity retention rate η_{cr} of Sn_{33.8}SiOCN (79.3%) is still better than that of Sn_{42.4}SiOCN electrode (76.9%). The magnesiation capacities delivered by Sn_{13.8}SiOCN and Sn_{20.1}SiOCN are 137.9 mAh/g and 151.3 mAh/g, respectively, which are much smaller than those of Sn_{33.8}SiOCN

Table 2. Overview of the first cycle magnesiation, demagnesiation, irreversible capacity and capacity retention rate (η_{cr}) under the current density of 0.5 mA/g, 50 mA/g and 500 mA/g.

Samples	Current density 0.5 mA/g				η_{cr} [%]
	$C_{mag.}$	$C_{demag.}$	C_{irr} [mAh/g]		
SiOCN	145.2	78.7	66.5		54.2
Sn _{13.8} SiOCN	293.0	240.6	52.4		82.1
Sn _{20.1} SiOCN	354.6	297.8	56.8		84.0
Sn _{33.8} SiOCN	420.2	362.2	58		86.2
Sn _{42.4} SiOCN	489.9	416.4	73.5		85.0
Samples	Current density 50 mA/g				
	$C_{mag.}$	$C_{demag.}$	C_{irr}		η_{cr} [%]
SiOCN	53.2	24.2	29		45.5
Sn _{13.8} SiOCN	137.9	104.3	33.6		75.6
Sn _{20.1} SiOCN	151.3	121.2	30.1		80.1
Sn _{33.8} SiOCN	172.9	137.1	35.8		79.3
Sn _{42.4} SiOCN	175.2	132.9	42.3		76.9
Samples	Current density 500 mA/g				
	$C_{mag.}$	$C_{demag.}$	C_{irr}		η_{cr} [%]
SiOCN	32.9	13.3	19.6		40.4
Sn _{13.8} SiOCN	98.3	68.7	29.6		69.9
Sn _{20.1} SiOCN	114.6	85.7	28.9		74.8
Sn _{33.8} SiOCN	136.6	104.1	32.5		76.2
Sn _{42.4} SiOCN	130.0	95.3	34.7		73.1

and $\text{Sn}_{42.4}\text{SiOCN}$. With a further increase in the current density to 500 mA/g, the magnesiation capacity and first cycle capacity retention rate η_{cr} for all electrodes further declined, which is due to the poor kinetics of Sn-based anodes that limit their capacities at high current density.^[33] However, $\text{Sn}_{33.8}\text{SiOCN}$ electrode shows both the highest magnesiation (136.6 mAh/g) and demagnesiation capacity (104.1 mAh/g), as well as the best first cycle capacity retention rate η_{cr} (76.2%). Although $\text{Sn}_{33.8}\text{SiOCN}$ has lower Sn content than the $\text{Sn}_{42.4}\text{SiOCN}$ nanocomposite, it possesses a higher surface area and free carbon content (see Table 1), and less agglomeration of Sn nanoparticles. These results suggest that the first cycle capacity retention rate η_{cr} and rate capability of Sn/SiOCN electrodes can be enhanced by controlling their surface area (i.e., porosity), as well as their content of metallic Sn and free carbon.

Since Mg^{2+} ion is smaller than Li^+ and Na^+ ions, it might follow the same storage mechanisms of the latter ions in the SiOCN matrix. These metal ions are usually stored in the micropores inside the SiOCN materials and then inserted into the SiOCN network.^[34–38] Consequently, more ions could be inserted in SiOCN network due to the expansion and the cleavage of some Si–C or Si–O bonds in their network resulting from the first insertion step.^[34] However, in comparison to Na^+ and Mg^{2+} ions, more Li^+ ions could be stored in SiOCN due to the favorable formation of Li-rich Si compounds and Li–Si alloys.^[39–41] Thus, incorporating Sn nanoparticles in the SiOCN matrix not only increases the capacity by alloying with magnesium but also enhances the magnesium ion insertion in the SiOCN network by facilitating the diffusion rate of Mg^{2+} ions, as also explained below.

Figure 4(e) compares the rate tests performance of SiOCN, $\text{Sn}_{13.8}\text{SiOCN}$, $\text{Sn}_{20.1}\text{SiOCN}$, $\text{Sn}_{33.8}\text{SiOCN}$ and $\text{Sn}_{42.4}\text{SiOCN}$ electrodes at different charge/discharge current densities. $\text{Sn}_{33.8}\text{SiOCN}$ shows the best performance among all anodes with a discharge capacity of 136.8 mAh/g in the 5th cycle at the current density of 50 mA/g, decreasing to 126.5, 115.8 and 104.7 mAh/g with increasing the current density to 100, 200 and 500 mA/g, respectively. These values are much higher than those of Sn-free SiOCN electrodes (i.e., 23.5, 19.0, 14.5 and 9.8 mAh/g at the current rate of 50, 100, 200 and 500 mA/g, respectively). Moreover, the discharge capacity of 21.8 mAh/g is recovered for $\text{Sn}_{33.8}\text{SiOCN}$ electrode when a low current density of 50 mA/g is reapplied at the end of the high current series.

To study the long-term stability of the anodes, the cycling performance of all electrodes was further examined for 100 cycles of galvanostatic charge/discharge at 500 mA/g. The ratio of the demagnesiation capacity C_{demag} in the 100th cycle

($C_{\text{demag},100}$) and in the 1st cycle ($C_{\text{demag},1}$) is named as the cycling stability coefficient η_{cs} (i.e., $C_{\text{demag},100}/C_{\text{demag},1} \times 100\%$). The ratio of C_{mag} in the n+1 cycle and C_{demag} in the n cycle is known as the coulombic efficiency η_{ce} (i.e., $C_{\text{mag},n+1}/C_{\text{demag},n} \times 100\%$). As shown in Figure 4(f) and Table S2, the Sn-containing samples ($\text{Sn}_{13.8}\text{SiOCN}$, $\text{Sn}_{20.1}\text{SiOCN}$, $\text{Sn}_{33.8}\text{SiOCN}$ and $\text{Sn}_{42.4}\text{SiOCN}$) show high cycling stability coefficient (i.e., $\eta_{\text{cs}} \geq 90\%$), which is much higher than that of the bare SiOCN anode (57.3%). The $\text{Sn}_{33.8}\text{SiOCN}$ anode possesses the highest stability, delivering a capacity of 101.8 mAh/g after 100 cycles with an excellent cycling stability coefficient of 96.8%. Besides, $\text{Sn}_{42.4}\text{SiOCN}$ anode shows a slightly lower cycling stability coefficient (93.6%) than that of $\text{Sn}_{33.8}\text{SiOCN}$ anode (94.5%). These results are consistent with other electrochemical performance results and might be explained by the lower surface area and lower free carbon content, as well as the high extent of Sn nanoparticle agglomeration in $\text{Sn}_{42.4}\text{SiOCN}$ nanocomposite compared with $\text{Sn}_{42.4}\text{SiOCN}$ and $\text{Sn}_{33.8}\text{SiOCN}$.

The long-term stability of $\text{Sn}_{33.8}\text{SiOCN}$ anode was further confirmed by SEM characterization before and after 100 cycles, as shown in Figure 5. From these figures, no obvious surface deterioration and structure collapse were observed, confirming the excellent cycling stability of $\text{Sn}_{33.8}\text{SiOCN}$ shown in Figure 4(f). The XRD characterization of the $\text{Sn}_{33.8}\text{SiOCN}$ anode after 100 cycles (see Figure S2) also reveals the stability of the metallic Sn crystallinity after 100 cycles of galvanostatic charge/discharge at 500 mA/g. These results indicate that the SiOCN matrix stabilizes Sn nanoparticles, reducing their volume expansion and agglomeration, and, in this way, preventing the electrode collapse after cycling.^[19]

The electrochemical kinetic characteristics of the electrode containing Sn and the electrode without Sn were examined using cyclic voltammetry (CV) measurements conducted at scanning rates of 0.1 mV/s, 0.5 mV/s, 1.0 mV/s, 2.0 mV/s and 5.0 mV/s, respectively. These measurements and relevant calculations are depicted in Figure 6. Based on the findings presented in earlier studies and the voltage profiles depicted in Figure 4(a–c), it is evident that electrodes containing Sn exhibit two distinct electrochemical peaks. These peaks occur at approximately 0.15 V (reduction) and 0.25 V (oxidation) on the cathodic and anodic sites, respectively, which can be attributed to the processes of magnesiation and demagnesiation of Sn.^[32,42] In contrast, evidently, the aforementioned peaks are not discernible in the Sn-free SiOCN electrode. With regard to the current response, for the same electrode sample, the sweeping integral area increases with the increase of current density. Moreover, samples presenting higher specific capacity in Fig-

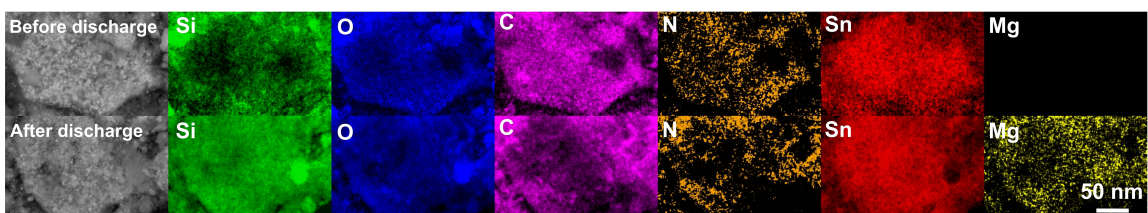


Figure 5. SEM–EDX mapping images of $\text{Sn}_{33.8}\text{SiOCN}$ electrode (a) before the first cycle and (b) after the 100th cycle.

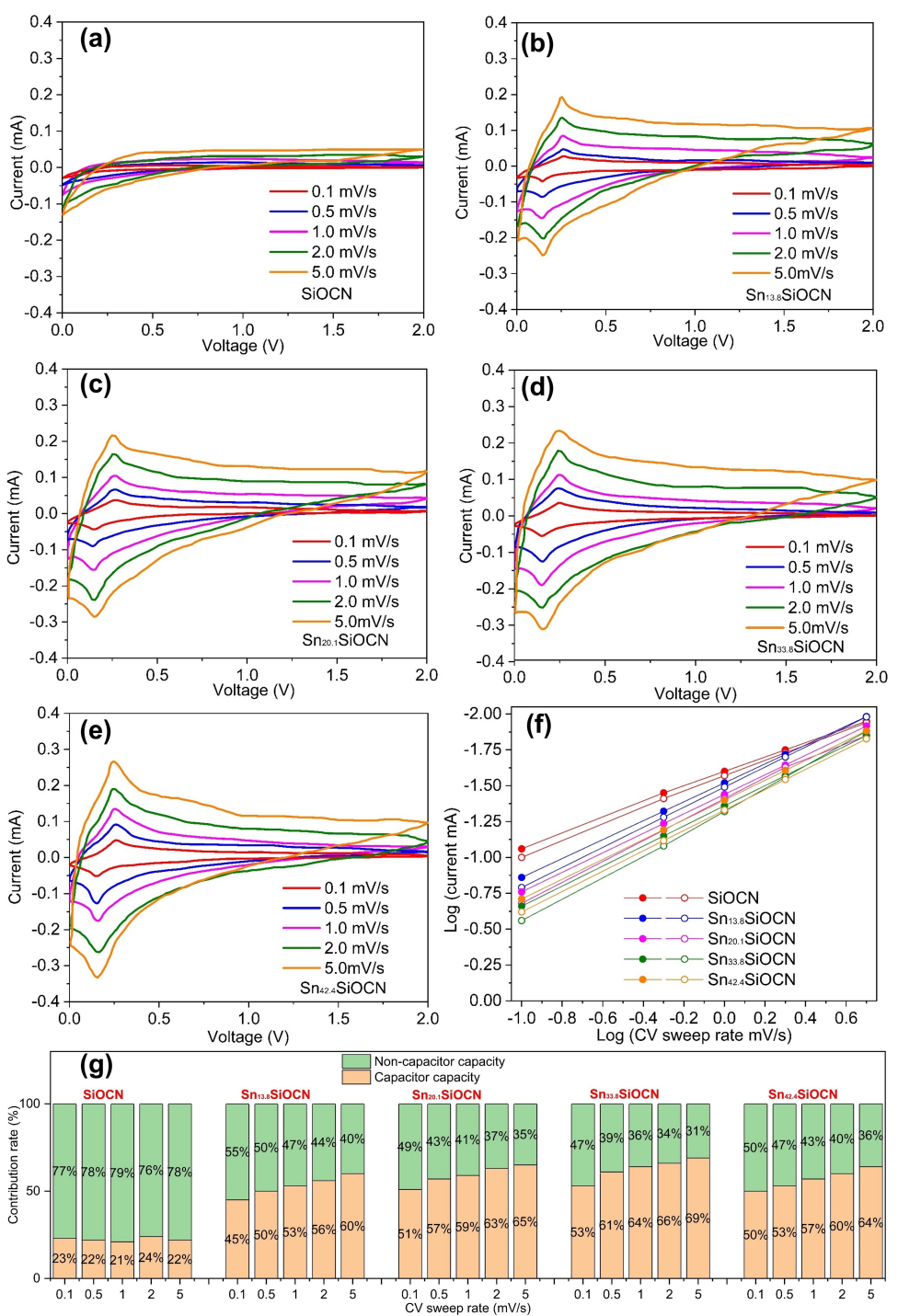


Figure 6. Cyclic voltammetry plots of (a) SiOCN; (b) Sn_{13.8}SiOCN; (c) Sn_{20.1}SiOCN; (d) Sn_{33.8}SiOCN; (e) Sn_{42.4}SiOCN (2nd cycle) at 0.1 mV/s, 0.5 mV/s, 1.0 mV/s, 2.0 mV/s and 5.0 mV/s; (f) The corresponding curves log i vs. log v for the cathodic (solid) and anodic (empty) peak; (g) The capacitor contribution in percentage at different scan rates.

ure 4 and higher tin content tend to show a higher current response area. For example, the sweeping integral area of Sn_{33.8}SiOCN and Sn_{42.4}SiOCN is apparently larger than that of SiOCN, Sn_{13.8}SiOCN and Sn_{20.1}SiOCN at the same sweeping rate. These results about CV current response are in accordance with the reference.^[43]

The elucidation of the electrode capacity contributions arising from both capacitor and non-capacitor behavior can be achieved by the analysis of cyclic voltammetry (CV) curves. Pseudo-capacitance refers to the capacitor-controlled activity characterized by faradaic charge transfer occurring on or near the surface region. This phenomenon exhibits qualities similar to a capacitor, enabling the achievement of rapid charge

storage.^[44,45] The dependence between the peak current (i) and the sweep rate (v) follows a power law, as represented by **Equation (1)**, whereby the adjustable parameters a and b are involved.^[46,47]

$$i = av^b \quad (1)$$

$b=0.5$ signifies non-capacitor behavior, whereas $b=1$ implies dominant capacitor behavior. Based on the analysis of Figure 6(f), the b values for the cathodic peak and anodic peak of SiOCN, Sn_{13.8}SiOCN, Sn_{20.1}SiOCN, Sn_{33.8}SiOCN and Sn_{42.4}SiOCN can be determined through the computation of the slope of log (i) against log (v) plots. The obtained b values for these materials are as follows: 0.53/0.56, 0.64/0.68, 0.70/0.73, 0.71/0.76, and 0.69/0.72, respectively. **Equation (2)** is the expression for the ratio of capacitor contribution, where k_1v denotes the capacitor contribution and $k_2v^{1/2}$ represents the contribution arising from non-capacitor processes. It is important to note that k_1 and k_2 are changeable constants, as referenced in sources.^[46,48]

$$i = k_1v + k_2v^{1/2} \quad (2)$$

$$i(V)/v^{1/2} = k_1v^{1/2} + k_2 \quad (3)$$

When dividing both sides of **Equation (2)** by $v^{1/2}$, **Equation (3)** is obtained. The determination of k_1 and k_2 was achieved by plotting $v^{1/2}$ versus $i/v^{1/2}$ at various scan rates, while maintaining a constant voltage. The slopes obtained from the plots were used to acquire the values of k_1 and k_2 . As depicted in Figure 6(g), the proportions of capacitor contribution for SiOCN, Sn_{13.8}SiOCN, Sn_{20.1}SiOCN, Sn_{33.8}SiOCN and Sn_{42.4}SiOCN at scan rates of 0.1 mV/s, 0.5 mV/s, 1.0 mV/s, 2.0 mV/s and 5.0 mV/s are 23%:22%:21%:24%:22%, 45%:50%:53%:56%:60%, 51%:57%:59%:63%:65%, 53%:61%:64%:66%:69% and 50%:53%:57%:60%:64%, respectively. By comparison, the influence of capacitor capacity was shown to be more significant in Sn-containing samples compared to Sn-free samples. As the concentration of Sn increases, there is a

corresponding increase in the capacitor contribution, with the exception of the Sn_{42.4}SiOCN nanocomposite. In the case of greater current densities (namely, 50 mA/g and 500 mA/g), this nanocomposite exhibits a somewhat lower value. The results demonstrate that the inclusion of Sn in the composition significantly enhances the battery's capacity. Additionally, the Sn_{20.1}SiOCN and Sn_{33.8}SiOCN compositions exhibit superior magnesiation-demagnesiation performance compared to Sn_{42.4}SiOCN, particularly at 50 mA/g and 500 mA/g (refer to Figure 4(a–c)). The capacitor contribution ratio of Sn-containing electrodes exhibits an upward trend as the scan rate increases, particularly for Sn_{33.8}SiOCN. For Sn-free SiOC electrode, the capacitor contribution remains nearly constant as the scan rate increases. The aforementioned findings demonstrate a strong correlation with the enhanced rate capability of samples containing tin (Sn), particularly the Sn_{33.8}SiOCN nanocomposite, which exhibits the highest rate capability as depicted in Figure 4(e).

EIS measurements were conducted for further investigation of the reaction kinetics. The EIS fitting curve and its corresponding equivalent circuit diagram are shown in Figure 7, and the impedance values are summarized in Table 3. The measurements were conducted before the first cycle and after the 100th cycle for comparison. The electrolyte resistance R_e is constant at approximately 1 Ω for all EIS measurements, which can be neglected for the total impedance. The semicircles in the high-frequency region represent the charge-transfer impedance between electrode-electrolyte interface (R_{ct}). The slopes in the low-frequency region represent the impedance of the Mg²⁺ ion diffusion process in the battery. In Figure 7(a), before the 1st cycle, Sn_{42.4}SiOCN and Sn_{33.8}SiOCN exhibit lower R_{ct} values, and SiOCN presents the highest R_{ct} value. The R_{ct} value decreases in the order of SiOCN>Sn_{13.8}SiOCN>Sn_{20.1}SiOCN>Sn_{33.8}SiOCN>Sn_{42.4}SiOCN, indicating higher Sn content within the samples could decrease the electrode-electrolyte impedance due to the high electrical conductivity of metallic Sn. Under lower current densities (i.e., 0.5 mA/g), the charge-transfer effects play a more important role than diffusion effects, which could explain the best performance of

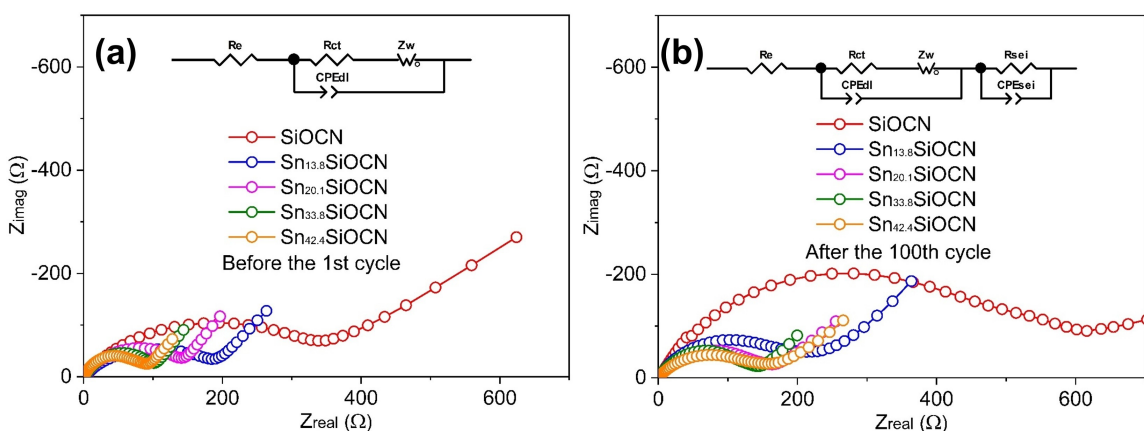


Figure 7. (a–b) Nyquist impedance plots and equivalent circuit models in the insets for SiOCN, Sn_{13.8}SiOCN, Sn_{20.1}SiOCN, Sn_{33.8}SiOCN and Sn_{42.4}SiOCN before the 1st cycle and after the 100th cycle (R_e is the electrolyte resistance, R_{ct} is the charge-transfer resistance, Z_w is the Warburg impedance, CPE_{dl} is the double layer constant phase element from the electrode, R_{sei} is the SEI film resistance, CPE_{sei} is the constant phase element from SEI film).

Table 3. Characteristic parameters from impedance spectra from EIS measurement and the relaxation voltage preceding EIS measurement.

Samples	Before the 1st cycle			After the 100th cycle		
	$R_{ct}(\Omega)$	$Z_w(\Omega)$	Total	$R_{ct} + R_{sei}(\Omega)$	$Z_w(\Omega)$	Total
SiOCN	336	621	957	619	938	1557
$\text{Sn}_{13.8}\text{SiOCN}$	186	313	499	239	421	660
$\text{Sn}_{20.1}\text{SiOCN}$	145	247	392	157	280	437
$\text{Sn}_{33.8}\text{SiOCN}$	118	225	343	135	251	386
$\text{Sn}_{42.4}\text{SiOCN}$	95	276	371	162	339	501

$\text{Sn}_{42.4}\text{SiOCN}$ shown in Figure 4(a).^[49] For the diffusion impedance, as shown in Figure 7(a), differences in slopes are clearly exhibited with the gradient decrease order of $\text{Sn}_{33.8}\text{SiOCN} > \text{Sn}_{20.1}\text{SiOCN} > \text{Sn}_{42.4}\text{SiOCN} > \text{Sn}_{13.8}\text{SiOCN} > 45^\circ > \text{SiOCN}$. According to the literature, when the gradient is closer to 90° , the diffusion process is closer to the ideal capacitor phenomenon,^[49] which means the $\text{Sn}_{33.8}\text{SiOCN}$ electrode exhibits the highest percentage of capacitor. The result is in good agreement with the CV results shown in Figure 6. The diffusion impedance can be calculated from the slopes based on **Equation (4):**^[50]

$$Z_w = \sigma\omega^{-1/2} - j\sigma\omega^{-1/2} \quad (4)$$

where ω is the angular frequency ($\omega = 2\pi f$), and σ is the Warburg coefficient (calculated from the slope of the line $Z' \sim \omega^{-1/2}$). After calculation, unlike the charge-transfer impedance, $\text{Sn}_{20.1}\text{SiOCN}$ and $\text{Sn}_{33.8}\text{SiOCN}$ present a smaller Z_w value, and SiOCN presents the highest Z_w value. The results imply that the diffusion impedance is not only affected by the Sn content of the samples but also by free carbon content and Sn aggregation extent. Compared with $\text{Sn}_{42.4}\text{SiOCN}$, the $\text{Sn}_{20.1}\text{SiOCN}$ and $\text{Sn}_{33.8}\text{SiOCN}$ nanocomposites exhibit higher surface area and free carbon contents, which provides more diffusion pathways. Besides, the high extent of Sn agglomeration in the $\text{Sn}_{42.4}\text{SiOCN}$ nanocomposite could also hinder ion diffusion. As shown in Table 3, the diffusion impedance of all samples before the 1st cycle is obviously higher than their charge-transfer impedance, meaning the diffusion impedance plays the dominant role, which could explain the better magnesiation-demagnesiation performance of $\text{Sn}_{20.1}\text{SiOCN}$ and $\text{Sn}_{33.8}\text{SiOCN}$ than that of $\text{Sn}_{42.4}\text{SiOCN}$ at 50 mA/g and 500 mA/g (see Figure 4(b–c)).

As shown in Figure 7(b), both the R_{ct} value and Z_w value of all cells increase after the 100th cycle. The results could be ascribed to shedding, inactivation, and corrosion of active materials and decomposition of electrolyte during cycling. Thus, the charge-transfer barrier increased, and the diffusion rate decreased. By comparison, the impedance of Sn-free SiOCN electrode is still much greater than that of Sn-containing SiOCN electrodes. However, the impedance of Sn-containing SiOCN electrodes is also increased by different extents. As shown in Table 3, the increase in total impedance of $\text{Sn}_{33.8}\text{SiOCN}$ is much lower than that of $\text{Sn}_{42.4}\text{SiOCN}$, which could be mainly ascribed to the higher surface area, free carbon content, less degree of Sn nanoparticles agglomeration in the $\text{Sn}_{33.8}\text{SiOCN}$ nanocompo-

sites compared to $\text{Sn}_{42.4}\text{SiOCN}$. Higher surface area, free carbon content, and uniform Sn distribution could help stabilize the electrode by providing more diffusion paths.^[18,22] The total impedance of all cells after the 100th cycle presents the increased order of $\text{Sn}_{33.8}\text{SiOCN} < \text{Sn}_{20.1}\text{SiOCN} < \text{Sn}_{42.4}\text{SiOCN} < \text{Sn}_{13.8}\text{SiOCN} < \text{SiOCN}$, which is in good accordance with the results of rate capability tests and cycling stability tests shown in Figure 4(e–f).

In order to confirm the alloying of Mg/Sn, assess the theoretical capacity, and evaluate the reversibility of the Sn-containing SiOCN electrode, ex-situ X-ray diffraction (XRD) measurements were performed on the $\text{Sn}_{33.8}\text{SiOCN}$ anode. These measurements were carried out at different discharge-charge states, while maintaining a current density of 0.5 mA/g. The appearance of reflections corresponding to the Mg_2Sn phase (identified as ICDD PDF#07-0274) was seen in Figure 8. This occurrence coincided with the completion of the discharging curve in the first cycle, specifically after the plateau at 0.15 V. Simultaneously, the reflections originating from metallic Sn were observed to be entirely absent, indicating the full alloying of metallic Sn with Mg^{2+} ions. This finding elucidates the strong concordance observed between the estimated discharge capacity (401.3 mAh/g) and the experimental discharge capacity (420.2 mAh/g) at a current density of 0.5 mA/g, as previously explicated. Upon recharging the battery following the plateau at around 0.25 V, the X-ray diffraction (XRD) pattern reveals the reappearance of metallic Sn reflection, whereas the reflections associated with Mg_2Sn totally vanish. The observed magnesiation plateau occurring at around 0.15 V can be attributed to the production of Mg_2Sn , as indicated by the electrochemical reaction represented by **Equation (5):**^[33]



The presence of a plateau at around 0.25 V signifies the extraction of Mg^{2+} from Mg_2Sn . This observation suggests that the storing mechanism of Mg^{2+} into the Sn/SiOCN material involves both capacitor behavior through micropores and intercalation with metallic Sn. The observations are consistent with prior studies that have examined Sn-based electrodes in the context of magnesium ion batteries.^[24,51,52] Furthermore, the voltage necessary for the extraction of Mg^{2+} from Mg_2Sn exhibited a mere 0.1 V increment in positivity compared to the voltage requisite for the insertion of Mg^{2+} into Sn. The observed low hysteresis indicates that the incorporation of Sn

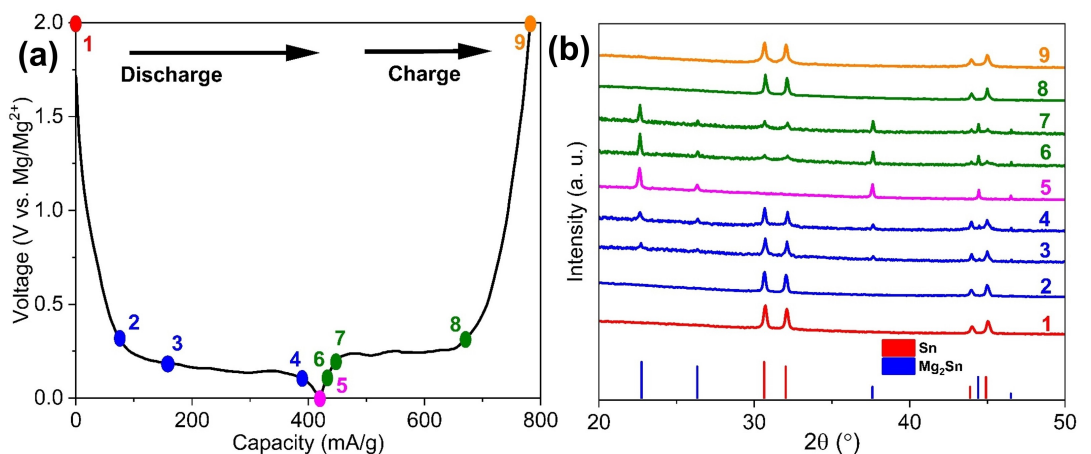


Figure 8. (a–b) The ex-situ XRD patterns of the $\text{Sn}_{33.8}\text{SiOCN}$ electrode at 0.5 mA/g during the 1st cycle. The reference patterns of metallic Sn (PDF #00–089–2958) and Mg_2Sn (PDF #00–007–0274) are shown at the bottom of the observed patterns.

into the SiOCN ceramic matrix could potentially mitigate electrode polarization and enhance battery performance, similar to the electrochemical findings reported earlier.^[53]

The $\text{Sn}_{33.8}\text{SiOCN}$ anode was further analyzed using X-ray photoelectron spectroscopy (XPS), as depicted in Figure 9 and Figure S3–S4 of the Supporting Information. As shown in Figure S3, the main peaks of Mg 1s and 2p orbitals are found at

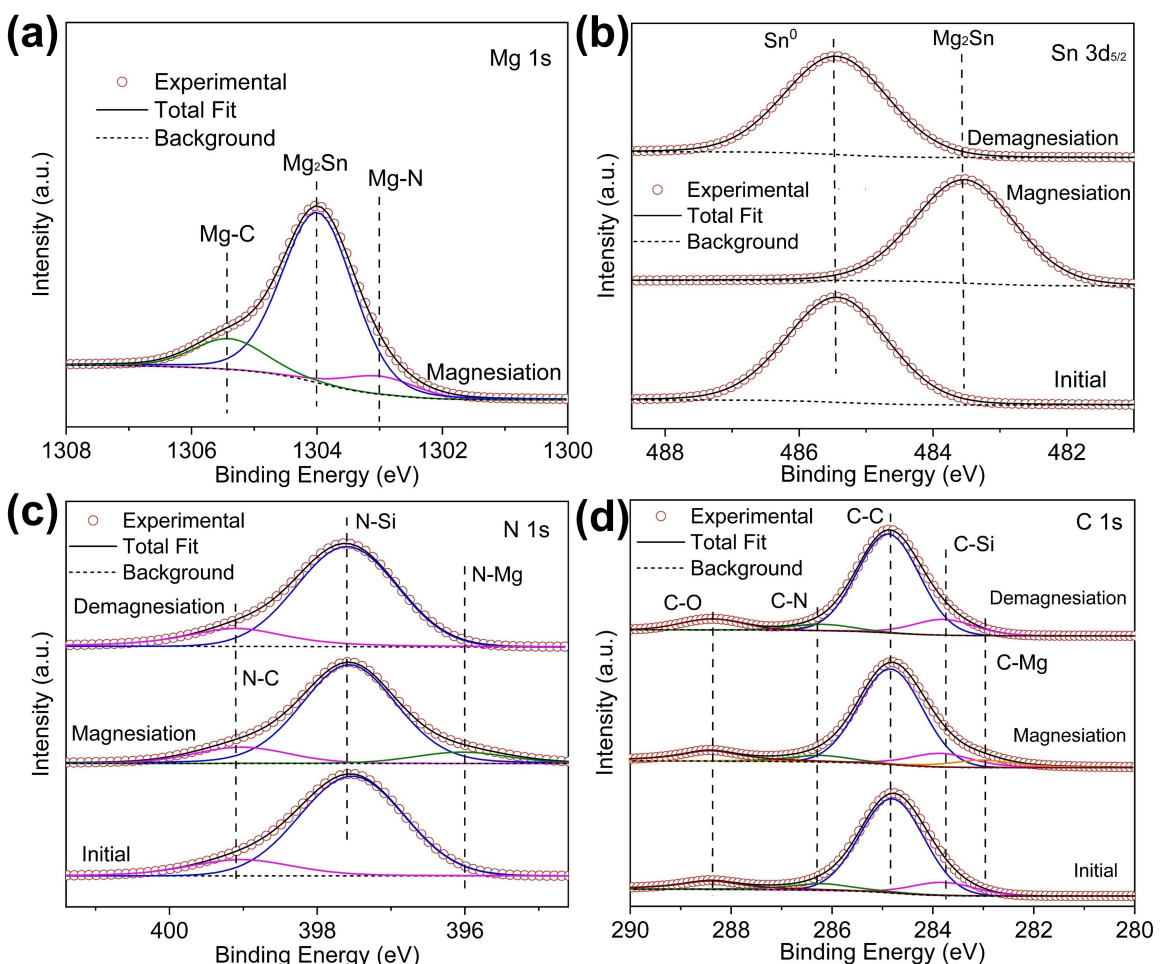


Figure 9. High-resolution (a) Mg 1s, (b) Sn 3d_{5/2}, (c) N 1s, and (d) C 1s X-ray photoelectron spectra of the $\text{Sn}_{33.8}\text{SiOCN}$ electrode at before and after magnesiation/ demagnesiation.

energy values of around 1304.0 eV and 49.7 eV, respectively, in the X-ray photoelectron spectra following the process of magnesiation. The observed main peaks, which are associated with the Mg₂Sn alloy,^[54,55] were no longer present following the demagnesiation of the battery. Furthermore, as illustrated in Figure 9a, the X-ray photoelectron spectra of Mg 1s of Sn_{33.8}SiOCN anode after magnesiation can be deconvoluted into three peaks at 1303.0 eV, 1304.0 eV and 1305.4 eV that can be assigned to Mg–N bond, Mg₂Sn compound, and Mg–C bond, respectively.^[56–59] The formation of Mg₂Sn is also confirmed by the shifting of the Sn 3d_{5/2} peak at 483.5 eV (Figure 9b) attributed to Sn⁰ in the initial anode prior to magnesiation to lower binding energy (485.3 eV) following the process of magnesiation, which corresponds to Mg₂Sn compound.^[24] The insertion of Mg ions in the SiOCN matrix is indicated by the appearance of an additional peak at 396.0 eV in the X-ray photoelectron spectra of N 1s (Figure 9c) of the anode after magnesiation, which can be assigned to N–Mg bond,^[57,58] while only two peaks at 397.5 and 399.1 eV corresponding to the N–Si and N–C bonds,^[60] respectively, are observed in the spectra of initial anode before magnesiation. Subsequently, upon demagnesiation, all the peaks corresponding to Mg bonding in the Sn/SiOCN anode disappeared, suggesting the reversibility of the electrochemical reactions between Mg and the anode materials. The findings support the ex-situ XRD data obtained from the magnesiation–demagnesiation cycle, as depicted in Figure 8. As shown in Figure 9d, the C 1s X-ray photoelectron spectra of Sn_{33.8}SiOCN anode before and after magnesiation / demagnesiation can be fitted with four peaks at 283.8 eV, 284.8 eV, 286.2 eV, and 288.4 eV, which can be assigned to C–Si, C–C, C–N, and C–O bonds, respectively.^[21] The additional peak at 283.0 eV in the magnesiation spectra of C 1s can be attributed to the C–Mg bond,^[59] indicating Mg ions also react with SiOCN and free carbon in the anode materials. The peak disappears in the C1s spectra after demagnesiation, which further demonstrates the reversibility of the reaction mentioned before. As shown in Figure S4, no remarkable changes are observed in the X-ray photoelectron spectra of Si 2p and O 1s before and after magnesiation/ demagnesiation, suggesting that Mg ions are mainly stored in Sn and N-doped free carbon in the Sn/SiOCN anode.

Conclusions

Sn-containing SiOCN nanocomposites anodes for magnesium ion batteries were synthesized and evaluated in this work. Results of battery performance tests show that the nanocomposite electrode (Sn_{42.4}SiOCN) presents a high first discharging capacity of 489.9 mA/g, 172.9 mA/g, and 136.6 mA/g at 0.5 mA/g, 50 mA/g and 500 mA/g, respectively. Apart from an exceptional rate performance efficiency of 76.5%, the Sn_{33.8}SiOCN anode was found to have a reversible capacity of 101.8 mAh/g after 100 cycles at a current density of 500 mA/g. The structure stability of the Sn_{33.8}SiOCN anode was confirmed by SEM–EDX mapping and XRD measurements before and after 100 cycling. CV experiments demonstrate an elevated tin

content enhances battery performance by increasing the share of capacitor capacity, with Sn_{33.8}SiOCN showing the highest capacitor capacity percentage. CV tests at different scan rates demonstrate that the increase in capacitor capacity is a contributing factor to the superior rate performance exhibited by Sn/SiOCN electrodes under higher current densities compared with tin-free SiOCN electrode. In EIS measurements, Sn_{33.8}SiOCN displays the lowest impedance of 386 Ω, which further demonstrates that an increased tin content leads to a notable enhancement in Mg²⁺ ion diffusion and battery performance by decreasing the impedance substantially. Ex-situ XRD showcases the synthesis of Mg₂Sn and the reversible electrochemical extraction/insertion of Mg²⁺ within the ceramic SiOCN matrix. Finally, the elemental binding energy shift of Sn/SiOCN was studied using X-ray photoelectron spectroscopy (XPS) in order to ascertain the significant contribution of Sn in enhancing battery performance. Besides, the battery performance was influenced by some other aspects, such as the accumulation of tin particles, the amount of free carbon present, and the specific surface area.

Author Contributions

WG Conceptualization, Methodology, Investigation, Data Curation, Writing–Original Draft. JW: Investigation. AG: Supervision, Writing–Review and Editing, Resources. MFB: Conceptualization, Investigation, Writing–Review and Editing, Supervision, Project administration. All authors have read and agreed to the published version of the manuscript.

Acknowledgements

Wuqi Guo acknowledges the financial support from the China Scholarship Council (201606280048). Open Access funding enabled and organized by Projekt DEAL.

Conflict of Interests

The authors declare no conflicts of interest.

Data Availability

The data that support the findings of this study are available from the corresponding author upon reasonable request.

Keywords: anode · energy storage · magnesium ion battery · Tin-containing Silicon oxycarbonitride

- [1] F. Duffner, N. Kronemeyer, J. Tübke, J. Leker, M. Winter, R. Schmuck, *Nat. Energy* **2021**, *6*, 123.
- [2] J. Muldoon, C. B. Bucur, T. Gregory, *Angew. Chem. Int. Ed.* **2017**, *56*, 12064.
- [3] J. Muldoon, C. B. Bucur, T. Gregory, *Chem. Rev.* **2014**, *114*, 11683.

- [4] A. Ponrouch, J. Bitenc, R. Dominko, N. Lindahl, P. Johansson, M. R. Palacin, *Energy Storage Mater.* **2019**, *20*, 253.
- [5] C. B. Bucur, T. Gregory, A. G. Oliver, J. Muldoon, *J. Phys. Chem. Lett.* **2015**, *6*, 3578.
- [6] M. Ge, C. Cao, G. M. Biesold, C. D. Sewell, S.-M. Hao, J. Huang, W. Zhang, Y. Lai, Z. Lin, *Adv. Mater.* **2021**, *33*, 2004577.
- [7] K. Kravchyk, L. Protesescu, M. I. Bodnarchuk, F. Krumeich, M. Yarema, M. Walter, C. Guntlin, M. V. Kovalenko, *J. Am. Chem. Soc.* **2013**, *135*, 4199.
- [8] M. Weiss, R. Ruess, J. Kasnatscheew, Y. Levartovsky, N. R. Levy, P. Minnemann, L. Stolz, T. Waldmann, M. Wohlfahrt-Mehrens, D. Aurbach, M. Winter, Y. Ein-Eli, J. Janek, *Adv. Energy Mater.* **2021**, *11*, 2101126.
- [9] Y. Sun, S. H. Guo, H. S. Zhou, *Adv. Energy Mater.* **2019**, *9*.
- [10] M. L. Mao, T. Gao, S. Y. Hou, C. S. Wang, *Chem. Soc. Rev.* **2018**, *47*, 8804.
- [11] X. Zhao, V.-P. Lehto, *Nanotechnology* **2021**, *32*, 42002.
- [12] Q. Wen, F. Qu, Z. Yu, M. Graczyk-Zajac, X. Xiong, R. Riedel, *Journal of Advanced Ceramics* **2022**, *11*, 984.
- [13] J. Rohrer, D. Vrankovic, D. Cupid, R. Riedel, H. J. Seifert, K. Albe, M. Graczyk-Zajac, *Int. J. Mater. Res.* **2017**, *108*, 920.
- [14] R. Riedel, G. Mera, R. Hauser, A. Klonczynski, *J. Ceram. Soc. Jpn.* **2006**, *114*, 425.
- [15] S. B. Mujib, G. Singh, *Int J Ceramic Eng Sci.* **2022**, *4*, 4.
- [16] M. Graczyk-Zajac, L. M. Reinold, J. Kaspar, P. V. Sasikumar, G.-D. Soraru, R. Riedel, *Nanomaterials* **2015**, *5*, 233.
- [17] J. Gonzalez, K. Sun, M. Huang, S. Dillon, I. Chasiotis, J. Lambros, *J. Power Sources* **2015**, *285*, 205.
- [18] J. Kaspar, C. Terzioglu, E. Ionescu, M. Graczyk-Zajac, S. Hapis, H.-J. Kleebe, R. Riedel, *Adv. Funct. Mater.* **2014**, *24*, 4097.
- [19] R. J.-C. Dubey, P. V. W. Sasikumar, F. Krumeich, G. Blugan, J. Kuebler, K. V. Kravchyk, T. Graule, M. V. Kovalenko, *Adv. Sci.* **2019**, *6*, 1901220.
- [20] D. H. Youn, A. Heller, C. B. Mullins, *Chem. Mater.* **2016**, *28*, 1343.
- [21] J. Wang, A. Gili, M. Grünbacher, S. Praetz, J. D. Epping, O. Görke, G. Schuck, S. Penner, C. Schlesiger, R. Schomäcker, A. Gurlo, M. F. Bekheet, *Materials Advances* **2021**, *2*, 1715.
- [22] J. Wang, D. Kober, G. Shao, J. D. Epping, O. Görke, S. Li, A. Gurlo, M. F. Bekheet, *Mater. Today* **2022**, *26*, 100989.
- [23] R. Bhandavat, Z. Pei, G. Singh, *Nanomaterials and Energy* **2012**, *1*, 324.
- [24] W. Q. Guo, O. Icini, C. Vakifahmetoglu, D. Kober, A. Gurlo, M. F. Bekheet, *Adv. Funct. Mater.* **2023**.
- [25] J. Wang, V. Schöchl, O. Görke, G. Schuck, X. Wang, G. Shao, S. Schorr, M. F. Bekheet, A. Gurlo, *Open Ceramics* **2020**, *1*, 100001.
- [26] C. Tan, J. Cao, A. M. Khattak, F. Cai, B. Jiang, G. Yang, S. Hu, *J. Power Sources* **2014**, *270*, 28.
- [27] L. van Nguyen, C. Zanella, P. Bettotti, G. D. Sorarù, *J. Am. Ceram. Soc.* **2014**, *97*, 2525.
- [28] W. Guo, D. A. H. Hanaor, D. Kober, J. Wang, M. F. Bekheet, A. Gurlo, *Batteries* **2022**, *8*.
- [29] E. Barrios, L. Zhai, *Molecular Systems Design & Engineering* **2020**, *5*, 1606.
- [30] B. Dong, Y. Han, T. Wang, Z. Lei, Y. Chen, F. Wang, H. Abadikhah, S. A. Khan, L. Hao, X. Xu, R. Cao, L. Yin, S. Agathopoulos, *ACS Appl. Energ. Mater.* **2020**, *3*, 10183.
- [31] F. Nacimiento, M. Cabello, C. Pérez-Vicente, R. Alcántara, P. Lavela, G. F. Ortiz, J. L. Tirado, *Nanomaterials* **2018**, *8*.
- [32] A. B. Ikhe, S. C. Han, S. J. R. Prabakar, W. B. Park, K.-S. Sohn, M. Pyo, *J. Mater. Chem. A* **2020**, *8*, 14277.
- [33] N. Singh, T. S. Arthur, C. Ling, M. Matsui, F. Mizuno, *Chem. Commun.* **2013**, *49*, 149.
- [34] C. Chandra, W. Devina, H. S. Cahyadi, S. K. Kwak, J. Kim, *Chem. Eng. J.* **2022**, *428*, 131072.
- [35] M. Weinberger, P.-H. Su, H. Peterlik, M. Lindén, M. Wohlfahrt-Mehrens, *Nanomaterials* **2019**, *9*.
- [36] J. Kaspar, M. Storch, C. Schitco, R. Riedel, M. Graczyk-Zajac, *J. Electrochem. Soc.* **2016**, *163*, A156-A162.
- [37] C. Chandra, J. Kim, *Chem. Eng. J.* **2018**, *338*, 126.
- [38] X. Dou, D. Buchholz, M. Weinberger, T. Diemant, M. Kaus, S. Indris, R. J. Behm, M. Wohlfahrt-Mehrens, S. Passerini, *Small Methods* **2019**, *3*, 1800177.
- [39] C. Chandra, H. S. Cahyadi, S. Alvin, W. Devina, J.-H. Park, W. Chang, K. Y. Chung, S. K. Kwak, J. Kim, *Chem. Mater.* **2020**, *32*, 410.
- [40] S. C. Jung, D. S. Jung, J. W. Choi, Y.-K. Han, *J. Phys. Chem. Lett.* **2014**, *5*, 1283.
- [41] C. Tang, Y. Liu, C. Xu, J. Zhu, X. Wei, L. Zhou, L. He, W. Yang, L. Mai, *Adv. Funct. Mater.* **2018**, *28*, 1704561.
- [42] W. He, K. Chen, R. Pathak, M. Hummel, K. M. Reza, N. Ghimire, J. Pokharel, S. Lu, Z. Gu, Q. Qiao, Y. Zhou, *Chem. Eng. J.* **2021**, *414*, 128638.
- [43] S. Eun Wang, J.-S. Park, M. Ji Kim, Y. Chan Kang, D. Soo Jung, *Appl. Surf. Sci.* **2022**, *589*, 152952.
- [44] P. Simon, Y. Gogotsi, B. Dunn, *Science* **2014**, *343*, 1210.
- [45] K. Yao, Z. Xu, M. Ma, J. Li, F. Lu, J. Huang, *Adv. Funct. Mater.* **2020**, *30*, 2001484.
- [46] P. Li, J.-Y. Hwang, Y.-K. Sun, *ACS Nano* **2019**, *13*, 2624.
- [47] K. Yao, Z. Xu, J. Huang, M. Ma, L. Fu, X. Shen, J. Li, M. Fu, *Small* **2019**, *15*, 1805405.
- [48] L. Shen, Y. Wang, H. Lv, S. Chen, P. A. van Aken, X. Wu, J. Maier, Y. Yu, *Adv. Mater.* **2018**, *30*, 1804378.
- [49] N. Meddings, M. Heinrich, F. Overney, J.-S. Lee, V. Ruiz, E. Napolitano, S. Seitz, G. Hinds, R. Raccichini, M. Gaberšček, J. Park, *J. Power Sources* **2020**, *480*, 228742.
- [50] W. Choi, H.-C. Shin, J. M. Kim, J.-Y. Choi, W.-S. Yoon, *J. Electrochem. Sci. Technol.* **2020**, *11*, 1.
- [51] M. Song, Y. Wang, C. Si, W. Cui, W. Yang, G. Cheng, Z. Zhang, *Science China Chemistry* **2022**, *65*, 1433.
- [52] M. Song, J. Niu, K. Yin, H. Gao, C. Zhang, W. Ma, F. Luo, Z. Peng, Z. Zhang, *Nano Res.* **2019**, *12*, 801.
- [53] B. Lu, Y. Song, Q. Zhang, J. Pan, Y.-T. Cheng, J. Zhang, *Phys. Chem. Chem. Phys.* **2016**, *18*, 4721.
- [54] G. Song, Y. Liu, L. Ran, Y. Shao, F. Hu, Y. Wu, H. Du, J. You, *Thin Solid Films* **2022**, *748*, 139175.
- [55] Y. He, T. Xia, C. Zhang, X. Zhao, *J. Solid State Electrochem.* **2023**, *27*, 3339.
- [56] S. Kim, N. -H. Kim, *IEEE Access* **2022**, *10*, 380.
- [57] N. Mao, J.-X. Jiang, *Appl. Surf. Sci.* **2019**, *476*, 144.
- [58] Z. Refaat, M. E. Saied Naga, Ahmed O. Abo El, S. A. Shaban, H. B. Hassan, M. R. Shehata, F. Y. E. Kady, *Environmental Science and Pollution Research* **2023**, *30*, 53817.
- [59] Q. Peng, Y. Dai, K. Liu, X. Luo, D. He, X. Tang, G. Huang, *J. Mater. Sci.* **2020**, *55*, 11267.
- [60] W. Zhao, G. Shao, S. Han, C. Cai, X. Liu, M. Sun, H. Wang, X. Li, R. Zhang, L. An, *J. Am. Ceram. Soc.* **2019**, *102*, 2316.

Manuscript received: January 18, 2024

Revised manuscript received: March 15, 2024

Accepted manuscript online: March 27, 2024

Version of record online: April 24, 2024